JOURNAL OF AIRCRAFT
Vol. 41, No. 3, May–June 2004

# Aeroelastic Analysis of Helicopter Rotor Blades on Deformable Chimera Grids

Hubert Pomin* and Siegfried Wagner†
*University of Stuttgart, D-70550 Stuttgart, Germany*

**Aeroelastic Reynolds-averaged Navier–Stokes and Euler computations are presented for an articulated model rotor in hover and forward flight. Comparative rigid-blade simulations are carried out to assess the effects of blade dynamics and elasticity on the numerical results. The INROT flow solver operates on deformable structured overset grids and can be tightly coupled with a finite element model of the rotor blade structure (DYNROT) based on Timoshenko beam theory. The order of time accuracy of fluid and structure modules is maintained in the overall analysis by an appropriate staggered coupling scheme. At the investigated thrust setting, global hover performance values computed by the coupled fully turbulent Navier–Stokes analysis agree fairly well with available experimental data. In forward flight, the aeroelastic results are in much better agreement with the measurements than those obtained from rigid-blade simulations with prescribed articulation. Apart from superior rotor power predicition, the local pitching moment coefficients computed by the viscous analysis are found to correlate better with wind-tunnel data than the corresponding Euler output.**

## Nomenclature

| | | |
|---|---|---|
| $b$ | = | number of rotor blades |
| $C_m M^2$ | = | pitching moment coefficient, $P/(0.5\rho_\infty c^2)$ |
| $C_n M^2$ | = | normal force coefficient, $N/(0.5\rho_\infty c)$ |
| $C_p$ | = | pressure coefficient, $(p - p_\infty)/[0.5\rho_\infty(r\lvert\boldsymbol{\omega}_{R1}\rvert + \sin\psi\lvert\boldsymbol{v}_{\mathrm{GR}}\rvert)^2]$ |
| $C_Q$ | = | torque coefficient, $Q/(\rho_\infty \pi R_{\mathrm{tip}}^3 M_{\mathrm{tip}}^2)$ |
| $C_T$ | = | thrust coefficient, $T/(\rho_\infty \pi R_{\mathrm{tip}}^2 M_{\mathrm{tip}}^2)$ |
| $C_X$ | = | force coefficient, $F_X/(0.5\rho_\infty \pi R_{\mathrm{tip}}^2 \lvert\boldsymbol{v}_{\mathrm{GR}}\rvert^2)$ |
| $C_Z$ | = | force coefficient, $F_Z/(\rho_\infty \pi R_{\mathrm{tip}}^2 M_{\mathrm{tip}}^2)$ |
| $c$ | = | local chord length |
| $\boldsymbol{E}, \boldsymbol{F}, \boldsymbol{G}$ | = | inviscid flux vectors |
| $\boldsymbol{E}_v, \boldsymbol{F}_v, \boldsymbol{G}_v$ | = | viscous flux vectors |
| FM | = | figure of merit, $C_T^{3/2}/(\sqrt{2}\cdot C_Q)$ |
| $F_X, F_Z$ | = | rotor force components |
| $M$ | = | local reference Mach number |
| $M_{\mathrm{tip}}$ | = | tip Mach number |
| $N$ | = | normal force per unit length |
| $n$ | = | time level |
| $\boldsymbol{n}$ | = | local surface normal vector |
| $P$ | = | pitching moment per unit length |
| $p$ | = | static pressure |
| $Q$ | = | rotor torque |
| $\boldsymbol{Q}$ | = | solution vector |
| $\boldsymbol{R}$ | = | right-hand-side vector |
| $Re_0$ | = | reference Reynolds number |
| $R_{\mathrm{tip}}$ | = | tip radius |
| $r$ | = | radial station |
| $\boldsymbol{r}, \boldsymbol{r}_\tau$ | = | coordinate, grid velocity vectors |
| $T$ | = | rotor thrust, static temperature |
| $\boldsymbol{v}, \boldsymbol{v}_{\mathrm{GR}}$ | = | relative flow velocity vector, forward flight speed |
| $x, y, z, t$ | = | physical coordinates |
| $\alpha_q$ | = | rotor shaft angle |
| $\beta, \zeta$ | = | blade flap, lag angle |
| $\theta, \theta_{1C}, \theta_{1S}$ | = | collective, cyclic blade pitch |
| $\Lambda$ | = | blade aspect ratio, $R_{\mathrm{tip}}/c_0$ |
| $\mu_t$ | = | eddy viscosity |
| $\xi, \eta, \zeta, \tau$ | = | generalized coordinates |
| $\rho$ | = | fluid density |
| $\sigma$ | = | geometric solidity, $bc_0/(\pi R_{\mathrm{tip}})$ |
| $\psi$ | = | blade azimuth angle |
| $\boldsymbol{\omega}_{R1}$ | = | angular velocity vector |

*Subscripts*

| | | |
|---|---|---|
| 0 | = | reference quantity |
| $\infty$ | = | freestream quantity |

*Superscript*

| | | |
|---|---|---|
| $*$ | = | dimensional quantity |

## Introduction

ROTORCRAFT flows rank among the most challenging applications in aerospace computational fluid dynamics (CFD). Whereas it is imperative to take into account the interactions of aerodynamics and structure dynamics in a simulation of the helicopter main rotor, even a stand-alone aerodynamic analysis is confronted with a huge spectrum of fundamental and interactional flow phenomena.[1]

Although the flow over an isolated hovering rotor is steady for a blade-fixed observer, computing this steady-state solution and, thus, predicting hover performance, a key issue in the design process of helicopters, represents a very demanding task. The complexity of the hover flowfield is primarily due to the close proximity of the rotor blades and strong vortical structures, which are convected away from the rotor disk at relatively low speeds, even at higher thrust settings. The tip vortex emitted by a lifting blade has a substantial impact on the effective local angles of attack in the outer region of its own and of the following blade. Consequently, the outcome of a numerical analysis intended to provide quantitative information on hovering rotor loads and performance depends largely on the ability of the procedure to predict the rotor wake system accurately.

In high-speed horizontal flight, unsteady three-dimensional transonic effects are dominant on the advancing side of the rotor and contribute significantly to the overall noise level of the helicopter [high-speed impulsive noise (HSI)], whereas regions of highly complex separated and reverse flow must be dealt with on the retreating

Received 24 July 2002; revision received 28 August 2003; accepted for publication 7 October 2003. 

*Research Assistant, Institute for Aerodynamics and Gasdynamics, Pfaffenwaldring 21. Member AIAA.

†Professor, Head, Institute for Aerodynamics and Gasdynamics, Pfaffenwaldring 21. Member AIAA.

side; the latter introduces a great deal of uncertainty into any current first-principles analysis based on Reynolds averaging. At lower advance ratios and especially in descent, massive blade vortex interaction (BVI) may occur, which affects the unsteady lift distributions of the blades and is also known to be a major source of rotor noise and helicopter vibration. Again, proper capture and conservation of the rotor wake is crucial for the success of the numerical analysis.

Over the past decade, numerous authors have presented and applied rotary wing Euler and Navier–Stokes codes, for example, Krämer,[2] Boniface and Sidès,[3] Stangl,[4] Wake and Baeder,[5] Wehr,[6] Strawn and Ahmad,[7] Beaumier et al.,[8] and Strawn and Djomehri.[9] In the aforementioned references, however, either rigid-blade behavior is assumed or, for hover computations, known blade deformations obtained from experiment or more elementary analysis tools are fed into the flow solver by a priori grid deformation.

In both hover and forward flight, the torsional response of the blade has a significant impact on the aerodynamic coefficients. In the forward flight regime, apart from the elastic twist, inadequate representation of especially the flapping motion of the articulated and/or elastic blade will produce incorrect local effective angles of attack, which result in inaccurate and possibly misleading results of the numerical analysis. Furthermore, the dynamic degrees of freedom are nonlinearly coupled.[10] Thus, rotary wings are systems of extreme complexity that require multidisciplinary solution strategies.

The partitioned procedures approach[11] maintains flow and structure solvers as entirely separate programs that exchange information along their common physical boundaries, the rotor blade surfaces, throughout the analysis. If the communication of the modules takes places on a per revolution basis, the procedure is refered to as a weak coupling approach, where the CFD output is used to correct iteratively and eventually eliminate the influence of a simplified aerodynamic model required in the structure solver. In recent years, this method has been applied by, for example, Servera et al.[12] and Pahlke and van der Wall.[13] In the strong coupling category, information between flow and structure solvers is exchanged on a per time step basis, and the CFD analysis is the sole and transient source of aerodynamic load information for the structure module, which consequently does not require a full a priori trim of the rotor based on external semi-empirical aerodynamics, for example, two-dimensional airfoil tables with corrections. Such a modular strong coupling procedure was developed for helicopter rotors by Hierholz[14] and Buchtala[15] by the use of the Euler flow model and was applied to hovering rotor test cases on periodic monoblock grids based on the Navier–Stokes equations by the present authors.[16]

High-resolution chimera grids are employed for strongly coupled numerical investigations. The objective of the present paper is to assess the ability of the aeroelastic analysis tool to capture the essential flowfield and blade dynamics characteristics and to quantify rotor performance data. The results are compared with uncoupled computations and available experimental data.

## Numerical Procedures

### Aerodynamics

INROT solves the Reynolds-averaged Navier–Stokes equations (RANS) in a steadily rotating frame of reference (Fig. 1) using absolute flow quantities.[2] A time-dependent transformation from physical to computational space is employed to permit arbitrary rigid and elastic motion of the rotor blades.

$$\frac{\partial \boldsymbol{Q}}{\partial \tau}+\frac{\partial \boldsymbol{E}}{\partial \xi}+\frac{\partial \boldsymbol{F}}{\partial \eta}+\frac{\partial \boldsymbol{G}}{\partial \zeta}-\frac{1}{Re_0}\left(\frac{\partial \boldsymbol{E}_v}{\partial \xi}+\frac{\partial \boldsymbol{F}_v}{\partial \eta}+\frac{\partial \boldsymbol{G}_v}{\partial \zeta}\right)=\boldsymbol{R} \quad (1)$$

To close the system of equations, perfect gas and Newtonian fluid properties are assumed, and for turbulent viscous cases, the Baldwin–Lomax[17] eddy viscosity model is applied. The cell-centered finite volume upwind scheme is based on an implicit time-discrete formulation of the governing equations providing up to third-order temporal accuracy, which is linearized via a Newton method. For the computation of the inviscid fluxes, an approximate

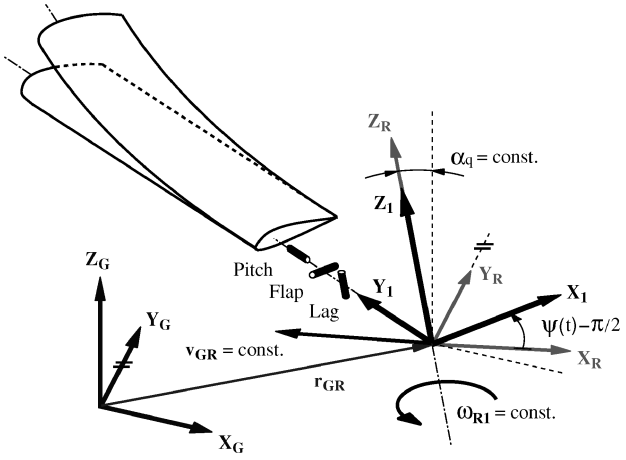


**Fig. 1 Key coordinate systems of aerodynamic formulation.**

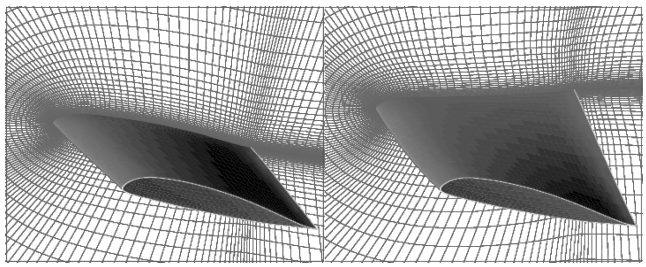

**Fig. 2 Undeformed/deformed blade and aerodynamic mesh section.**

Riemann solver is applied in conjunction with Eberle's low dispersion scheme,[18] which ensures up to third-order spatial accuracy in computational space. The viscous fluxes are computed using second order central differences and a lower–upper symmetric Gauss–Seidel (LU-SGS) operator according to Jameson and Yoon[19] is applied to integrate the system in time. Details regarding the numerical algorithm may be found in Refs. 6 and 16.

### Blade Kinematics

Pitch, flap, and lag hinges are included in the aerodynamic analysis to ensure an accurate representation of the blade kinematics for articulated rotors in both plain aerodynamic and aeroelastic simulations (Fig. 1). The individual hinge coordinates, and thus the sequence of the elementary transformations, are provided to the flow solver as input parameters. Once the evolving overall transformation operator is set up at execution start, the position of the blade roots relative to the reference system can be determined before each time step based on the present hinge angles. In a stand-alone CFD analysis, these quantities are functions of the blade azimuth angle $\psi$ with prescribed harmonic coefficients, whereas in a coupled simulation, the hinge angles are, along with elastic deformation, provided by the dynamics module.

### Deformable Grids

For aeroelastic computations, a robust algebraic grid deformation tool utilizing Hermite polynomials is applied before each time step to update the structured aerodynamic mesh according to surface deformation provided by the structure solver. At present, the deformed surface is determined by bending and twisting the blade quarter-chord line only. However, as shown in Fig. 2, the deformation algorithm is capable of dealing with variable camber and can remain in its present form for future investigations with more sophisticated dynamics models that call for flexible blade section shapes. To minimize the amount of grid deformation and, thus, maintain a high level of grid quality, the entire virgin grid is rotated into the root-tip secant of the deformed quarter-chord line before updating the three-dimensional grid according to the current deformed blade surface.

#### Laminar–Turbulent Transition

Typical model rotor blades feature vast regions of laminar flow, especially on the lower surface. Thus, the assumption of a fully turbulent boundary layer may lead to a significant overestimation of drag in a rotary wing Navier–Stokes computation. Because turbulence models are in most cases unable to predict transition locations reliably, this information is taken from experimental data and/or other numerical approaches and can be provided to the INROT flow solver before the computation for an arbitrary number of radial stations and, for unsteady cases, azimuthal locations. The external data are then interpolated to provide transition locations along the entire discretized blade span and at all discrete blade azimuth angles.

Throughout the computation, $\mu_t = 0$ is enforced in the time-dependent designated laminar region along the blade surface. The prescribed transition feature is only applied in a comparative hover computation to quantify its influence on rotor performance.

#### Boundary Conditions

A minimum of two ghost cell rows is added at all six faces of a given grid block, and the conservative variables in these virtual cells are prescribed before each Newton iteration according to the respective boundary type. Along solid walls, an inviscid flowfield representation must satisfy the slip wall condition $(\boldsymbol{v} - \boldsymbol{r}_\tau)\boldsymbol{n} = 0$. For viscous flows, the no-slip condition must hold, and the heat flux through a solid surface is forced to zero, that is $\boldsymbol{v} - \boldsymbol{r}_\tau = 0$ and $\partial T / \partial \boldsymbol{n} = 0$. A number of additional boundary procedures apply to special grid and flow requirements. These are briefly described in the following paragraphs.

#### Chimera Approach

Domain reduction using periodic grids[20] is limited to axial cases, whereas the overset grid approach (Fig. 3) is applicable to the entire helicopter flight spectrum. The INROT chimera implementation was originally developed and applied with the Euler flow model by Stangl[4] and Wehr.[6] Rotating body-fitted blade grids undergoing arbitrary motion are embedded in a common space-fixed cylindrical or Cartesian background grid, and a trilinear interpolation procedure is applied for the exchange of flow information along the chimera boundaries. Details regarding the procedure are included in Refs. 4, 6, and 16.

Whreas the blade grids provide adequate resolution to compute viscous flow, this feature must be compromised for the background grid due to memory and CPU restrictions. Therefore, a RANS solution is computed on the blade grids only, whereas the Euler model, fully capable of convecting the rotor wake, is used on the background mesh. The resulting procedure is refered to as hybrid analysis. To minimize wall clock computing time, the background grid is internally decomposed. All internal grid blocks can be processed in parallel.

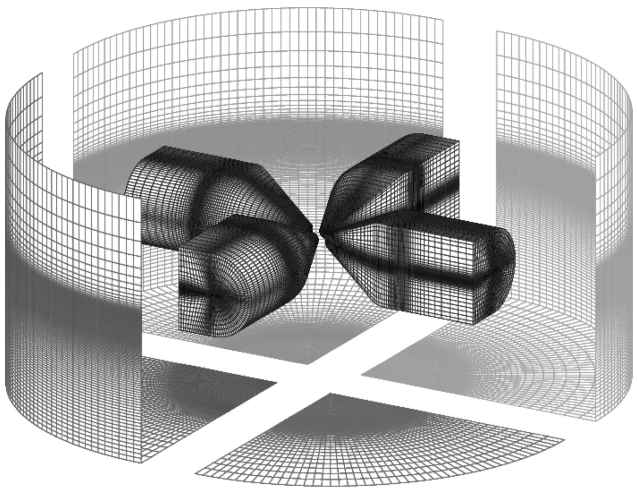

**Fig. 3 Exemplary chimera rotor grid configuration.**

#### Hover Boundary Conditions

Prescribing undisturbed flow along the far-field boundary in hover analyses is known to cause disturbing recirculation effects unless a very large distance ($\gg 3R_{\text{tip}}$) is available between the investigated rotor geometry and the far-field boundary. In this paper, classic one-dimensional momentum theory is applied in conjunction with a three-dimensional sink to determine in- and outflow velocities along the outer boundaries of the domain. Similar procedures were published, for example, by Beaumier et al.[8] and Strawn and Ahmad.[7] The rotor thrust coefficient required for the application of the momentum theory is obtained by integrating the surface forces of all rotor blades. A three-dimensional sink is positioned at the center of the rotor disk, and the source strength is adjusted to balance the mass outflow. Thus, inflow velocity vectors pointing toward the hub can be defined along the remainder of the far-field boundary as a function of hub distance, rotor thrust, blade-tip velocity, and tip radius.[7,16] With the computed velocities, the corresponding density and total energy values can be found via isentropic relations and the equations of state. The procedure is initialized by use of either a prescribed, for example, measured, rotor thrust or by the assumption that $C_T = 0$. By linear blending, the influence of the initial thrust value is gradually eliminated within a given number of time steps.

#### Blade Dynamics

In DYNROT, the rotor blade is modeled as a quasi-one-dimensional and, at present, geometrically linear Timoshenko beam. In contrast to an Euler–Bernoulli beam, the Timoshenko model takes into account the rotatory inertia of the blade sections and possible shear deformation of the rotor blade. The equations of motion are obtained analytically via an extended form of Hamilton's principle for nonconservative systems and are solved using the generalized-$\alpha$ method proposed by Chung and Hulbert.[21] A broader perspective on the structure model is available in Ref. 15.

## Fluid–Structure Coupling

Fluid and structure solvers are maintained as entirely individual programs on seperate computers, which communicate via socket connections and exchange information throughout the computation along their common physical boundary, the rotor blade surface. The partitioned procedures approach greatly simplifies code development and management. Higher-order accuracy in time can be preserved, provided a suitable coupling scheme is employed. In the present work, an implicit–implicit scheme developed by Hierholz[14] and Buchtala[15] is used.

1) Aerodynamic loads of time level $t^n$ are sent to the structure module.

2) Structure state is integrated from $t^{n-1/2}$ to $t^{n+1/2}$ using the midpoint rule.

3) Surface coordinates at time level $t^{n+1}$ are determined in the predictor step.

4) Surface coordinates of time level $t^{n+1}$ are sent to the fluid module.

5) There is grid deformation, as well as calculation of surface velocities at $t^{n+1}$ according to Geometric Conservation Law (GCL) and time integration of RANS/Euler equations to $t^{n+1}$.

This staggered coupling algorithm features an offset of half a time step between fluid and structure integration and can provide second-order accuracy in time for the overall method.[15]

## Results and Discussion

The aeroelastic chimera analysis is applied to generate an extensive numerical database for popular hover and forward flight test cases of the four-bladed ONERA/Eurocopter 7A model rotor, which has a diameter of $2 \times R^{\star}_{\text{tip}} = 4.2$ m and a geometric solidity of $\sigma \approx 0.0849$. The fully articulated 7A blades are characterized by an aspect ratio $\Lambda = 15$, a rectangular planform, a square tip, and feature a linear aerodynamic twist of $-3.95$ deg/m and a prelag of $-4$ deg. The lag, flap, and pitch hinges are located at (0.0357, 0.0362, and 0.0743) $\times R_{\text{tip}}$. Experimental data are available to assess the quality of the computed solutions.

### 7A Rotor in Hover

The hover test case computed for the present paper is defined by $\theta_{0.7} = 7.46$ deg, $M_{\text{tip}} = 0.617$, $\rho_\infty^\star = 1.18$ kg/m$^3$, and $T_\infty^\star = 298$ K, which result in significant compressibility and a Reynolds number of approximately $1.92 \times 10^6$ at the blade tips.

Each C–H type rotor blade grid features $203 \times 101 \times 83$ points in the wraparound, spanwise, and normal directions, respectively (53 points normal for Euler), which results in a total of approximately 1,660,000 cells, including all required boundary cell rows (Euler, approximately 1,050,000). The blade surface is discretized using $133 \times 71$ points with a minimum wall normal spacing of approximately $1.2 \times 10^{-5} \times c$ (chord length) for Navier–Stokes and $1.0 \times 10^{-3} \times c$ in the Euler analysis. In the viscous computations, a maximum $y^+$ of approximately 1.0 is observed near the leading edge in the tip region, which indicates a suitable resolution of the boundary layer for the algebraic turbulence model used. In both grids, radial spacing of the C sections is reduced to $5.0 \times 10^{-2} \times c$ at the blade tip to allow for adequate tip vortex resolution. In all directions, the outer boundaries of the blade grids are located at a distance of approximately $1.5 \times c$ and $3.0 \times c$ from the blade root and tip, respectively.

All blade grids are embedded in a nonrotating cylindrical background grid (Fig. 3) with $199 \times 208 \times 210$ points in the azimuthal, radial, and vertical directions. A cylindrical topology is chosen for the hover investigations. Radial and vertical spacing around $r = R_{\text{tip}}$ and $z = 0$ is set to $3.125 \times 10^{-2} \times c$, and the outer grid boundaries are located at $r = 3.1 \times R_{\text{tip}}$ and $z = \pm\, 1.7 \times R_{\text{tip}}$ (not including far-field boundary cells). For nearly load-balanced parallel processing, the background grid is internally subdivided into four blocks of equal size with point-to-point overlaps, which results in a total of approximately 9,200,000 background grid cells including all required boundary rows. Thus, the overall chimera hover grid system for hybrid Euler/Navier–Stokes computations consists of approximately 15,800,000 cells. The selected computational time step of the unsteady hybrid as well as the Euler hover simulations is equivalent to an azimuth increment of $\Delta\psi = 1.0$ deg. On 8 vector processors of a NEC SX-5 supercomputer, the overall CPU time per rotor revolution, that is, per 360 time steps, of the viscous analysis amounts to approximately 41 h at close to $11.5 \times 10^9$ floating-point operations per second (GFLOPS).

The global rotor coefficients are time averaged over the final four revolutions of the computations and are compared in Fig. 4 with experimental data that were also used in Ref. 16. Another measured hover polar for the 7A rotor at identical test conditions can be found in Ref. 8 and is represented by the lower limits of the white bars. The apparent error bands cannot be discussed here because the authors of the present paper have no background information on the differing experimental data sets. The computed thrust values of both the hybrid Navier–Stokes/Euler and the pure Euler chimera calculations correlate well with the experimental databand. The $C_T$ ratio of Euler over hybrid is 1.010 and 1.015 in the aerodynamic and aeroelastic simulations, respectively. Inclusion of the blade dynamics and elasticity is found to reduce the thrust coefficient by 2.7% (hybrid) and 2.1% (Euler) compared to the uncoupled analysis. This thrust reduction is almost exclusively due to the moderate torsional deformation of the fairly stiff 7A blades. The incorporation of laminar–turbulent transition leads to a thrust reduction of approximately 1.7% compared to the results of the fully turbulent coupled simulation. The effect of laminarity on the predicted torque coefficient is much more pronounced, approximately −7.7%. As expected, this reduction is primarily due to a 30% decrease in skin-friction-induced rotor torque, whereas the decrease of the pressure contribution corresponds roughly to the observed thrust reduction. In the fully turbulent calculations, the overall torque computed by the coupled analysis is approximately 5.5% lower than the corresponding value of the plain aerodynamic simulation, whereas the torque contributions due to skin friction remain almost constant. The hybrid aeroelastic simulation converges to a slightly higher rotor figure of merit compared to the rigid-blade analysis (approximately one point) and both values agree fairly well with the measured rotor performance, whereas the inclusion of laminar–turbulent transition

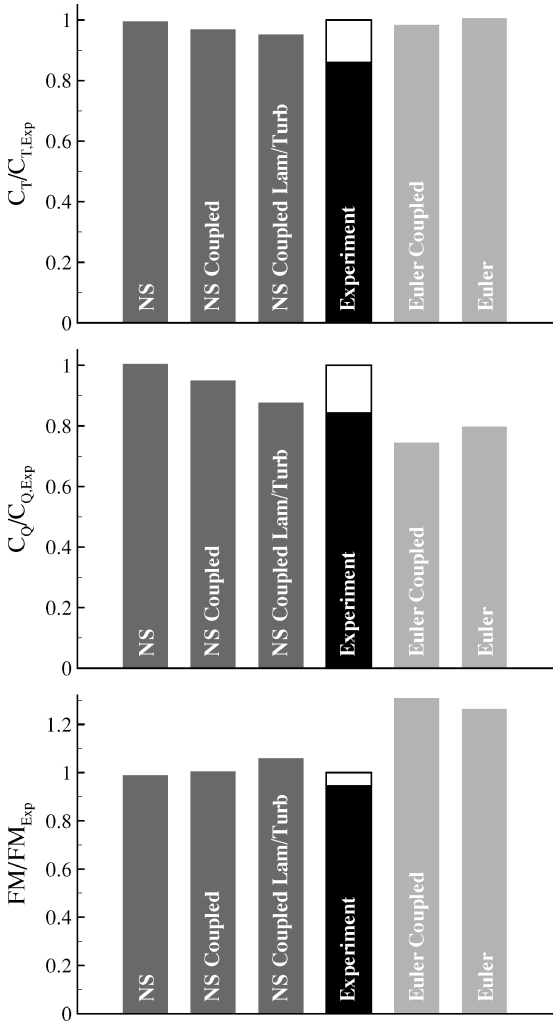


**Fig. 4 Comparison of hover performance data.**

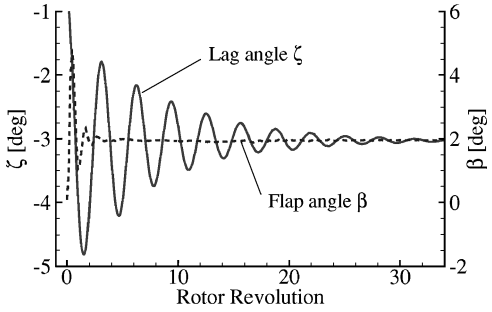


**Fig. 5 Time history of flap and lag angles.**

leads to an increase of the figure of merit of almost four points and, thus, to a quite significant overestimation compared to experiment. Similar observations were reported by d'Alascio et al.[22] This overestimation may be due in part to the omission of the rotor hub structure in the present numerical analysis, possible inaccuracies regarding the transition points provided to the flow solver, and/or the limited applicability of the quasi-two-dimensional algebraic eddy viscosity model.

Figure 5 shows the time history of the flap and lag hinge angles in the coupled fully turbulent viscous simulation, where these degrees of freedom are part of the numerical solution. The frequency of the observed lag motion is approximately $0.32 \times |\omega_{R1}|$, which is close to the lag eigenfrequency of a typical articulated rotor blade. This oscillation probably is the result of the instantaneous acceleration of the rotor to the full hover speed at the beginning of the numerical

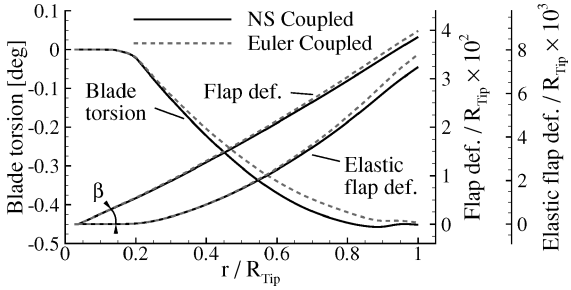


**Fig. 6 Computed blade deformation in hover.**

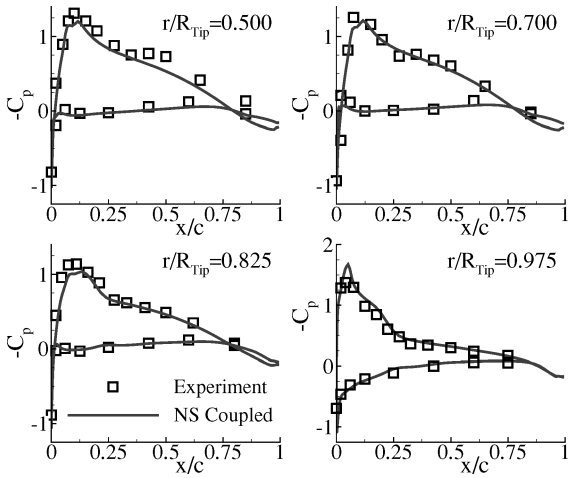


**Fig. 7 Pressure coefficients.**

analysis, which excites the entire frequency spectrum. The very low damping of the lag mode corresponds to a logarithmic decrement of approximately 0.4, whereas the flap damping is high, which causes the large initial flap amplitudes nearly to vanish within about 5 rotor revolutions.

The computed elastic deformation of the rotor blades is shown in Fig. 6. Consistent with the less distinct reduction of rotor thrust mentioned earlier, the torsional deformation predicted by the Euler analysis is smaller over most of the blade span compared to the viscous model. Although not visible in Fig. 6, both curves feature a horizontal tangent at the blade tip. The Euler tip flap deflection is slightly higher than the respective value of the hybrid computation, which is due to higher sectional thrust resulting from the more pronounced transonic effects at the blade tip in the inviscid analysis and the coupling of the flap bending and torsional degrees of freedom. The elastic flap contribution is shown separately to highlight the strong influence of the centrifugal forces in the tip region.

Pressure distributions computed with the fully turbulent hybrid analysis are plotted in Fig. 7 for a number of radial stations. Good agreement of the numerical results with experimental data obtained in the framework of the BRITE–EURAM HELISHAPE project[23] is achieved, with minor deviations in the rear portion of the suction side at 50% tip radius and a slight overestimation of the suction peak near the blade tip.

A portion of the complex wake structure of the hovering rotor is shown in Fig. 8, where the $\lambda$ criterion[24] is used to visualize the tip vortices. The contraction of the rotor wake is clearly visible, and, up to the first blade passage, almost no widening of the tip vortex core can be detected. Interaction of the vortex with the following blade leads to a significant increase of the core diameter and also appears to trigger secondary vortices. At 90-deg age, the center of the tip vortex core is found to pass slightly below the blade at approximately $(0.92\text{–}0.93) \times R_{\text{tip}}$.

In Fig. 9, contours of the computed vorticity magnitude in the blade grid are mapped on a vertical plane 10 deg behind the rotor blade. The shear layer behind the blade is distorted by the interacting tip vortex of the preceding blade and the streamribbons serve to illustrate the up- and downwash velocities induced by the two

**Table 1 Primary rotor control parameters**

| Trim tools | $\alpha_q$ | $\theta_{0.7}$ | $\theta_{1C}$ | $\theta_{1S}$ |
|---|---|---|---|---|
| HOST rigid | −12.72° | 8.83° | 1.67° | −3.46° |
| HOST elastic | −12.07° | 10.19° | 0.86° | −3.31° |
| Experiment | −13.75° | 10.41° | 3.43° | −3.70° |

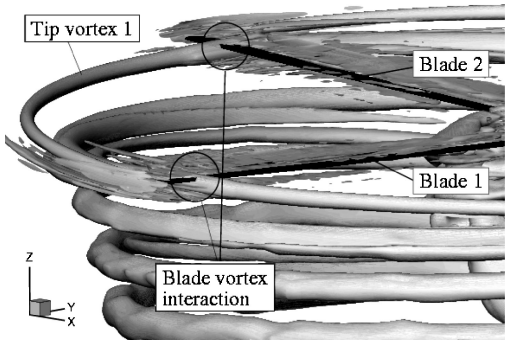


**Fig. 8 Section of computed wake structure.**

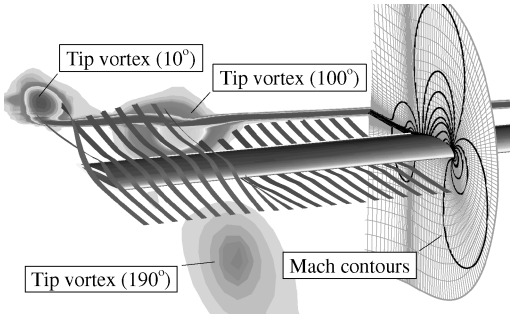


**Fig. 9 Streamtraces and vorticity magnitude 10 deg behind blade.**

youngest tip vortices. The fairly large core diameter of the blade grid representation of the 190-deg wake age vortex is in part due to the blade passage 90-deg earlier, but presumably also a result of the multiple chimera interpolations and the increasingly coarse vertical spacing of the blade grid below the rotor disk, as indicated by the grid section included in Fig. 9.

### 7A Rotor in Forward Flight

The specifications of the high-speed forward flight test case are $M_{\text{tip}} = 0.656$, $\mu = 0.4$, and a tip rotation Reynolds number of approximately $2.14 \times 10^6$. Given in components of the wind-tunnel system, the global rotor force coefficients obtained in the S1 Modane experiments (see Ref. 12) are $200 \times C_Z/\sigma = 12.56$ and $C_X/\sigma = 0.1$.

The primary rotor control parameters, that is, the shaft tilt angle $\alpha_q$ and the blade pitch $\theta(\psi)$, must be known to define fully the aeroelastic simulation. Whereas these quantities could be retrieved directly from the experimental logs, it must be considered that the isolated rotor analysis does not take into account wall and support pertubations of the wind-tunnel experiment that are known to have a significant influence on rotor trim and performance. Therefore, new sets of control parameters are computed using the comprehensive helicopter simulation tool HOST[25] based on the earlier trim objective. HOST features blade element theory aerodynamics and models the blade as a geometrically nonlinear multibody system. The trim results obtained for the rigid-blade stand–alone CFD and the aeroelastic computations are given in Table 1 along with the experimental values. Freezing the elastic degrees of freedom is found to result in a trim state that differs significantly from the output of the elastic blade calculation, and it should be kept in mind that both results must formally be regarded as initial solutions of an iterative trim process due to the simplified aerodynamics in HOST. Apart from the given parameters, a stand–alone CFD analysis also requires the prescription of the blade flap and lag angles $\beta(\psi)$ and $\zeta(\psi)$, respectively, which are available as part of the HOST solution. Whereas

the impact of the lag motion on the blade loads is minor, omission of the flap mode will provide totally misleading results, as will be shown later.

For the forward flight computations, the same blade grids as for the hovering rotor studies are used, whereas a modified cylindrical background grid with $199 \times 238 \times 177$ points is generated with a smaller vertical range of high resolution compared to the hover grid because of the fairly high advance ratio. Additional points are inserted in radial direction to improve conservation of the forward flight vortex system. A Cartesian background grid with $451 \times 397 \times 177$ nodes, similar far-field boundary locations, and identical grid point distribution up to the blade tips is tested to quantify the influence of the background mesh topology on the unsteady blade loads. The Cartesian grid is internally subdivided into 12 blocks of equal size in computational space.

Fully turbulent flow is assumed in the initial hybrid forward flight computations and the azimuthal increment per time step is set to $\Delta\psi = 0.5$ deg for Euler and Navier–Stokes. The total number of grid cells in the hybrid analysis amounts to 15,600,000 (cylindrical background grid) and 42,600,000 (Cartesian background grid), respectively. Key performance data of typical hybrid computations on a NEC SX-5 is included in Table 2. The computations with the 12 fairly small internal Cartesian background grid blocks outperform those on the cylindrical grid primarily because the partly unvectorizable chimera transfer operations are distributed on a larger number of processors for parallel execution. Furthermore, the whole completion procedure is found to require fewer iterations on the Cartesian grid. However, the cylindrical grid is used for the majority of the forward flight computations due to limited computing resources.

In Fig. 10, the time history of the overall rotor thrust computed by the aeroelastic hybrid analysis is plotted along with the lag angle of the first blade. At the beginning of the computation, the lag motion exhibits a behavior similar to that observed in the coupled hover simulations, which is again attributed to the instantaneous acceleration of the rotor blades in the numerical analysis and the very low damping of the lag mode. As the amplitude of the 1/3 per revoltution oscillation decreases, the contributions of higher frequencies become more distinct, and these authors anticipate that, eventually, the $\zeta(\psi)$ solution will only feature contributions of 1/revoltution and higher. The reflection of the low-frequency lag oscillation in the computed global rotor thrust is clearly visible, and all coupled results presented subsequently are, therefore, averaged over several rotor revolutions. In the plain aerodynamic computations, 2–3 revolutions are sufficient to obtain a periodic solution.

The time-averaged global rotor coefficients computed by the coupled and uncoupled CFD simulations with the cylindrical background grid, as well as the corresponding values of the HOST trim calculations and the wind-tunnel tests, are plotted in Fig. 11, where $C_X$ and $C_Z$ are the nondimensional force components in the upstream and vertical tunnel directions, respectively. The stand-alone CFD computations with prescribed pitch, flap, lag, and rotor shaft

**Table 2 Performance data of hybrid analysis**

| Background grid | Number of CPUs | CPU, h per revolution | GFLOPS | Memory, GB |
|---|---|---|---|---|
| Cylindrical | 8 | 80 | 11.5 | 8.1 |
| Cartesian | 16 | 171 | 27.0 | 23.5 |

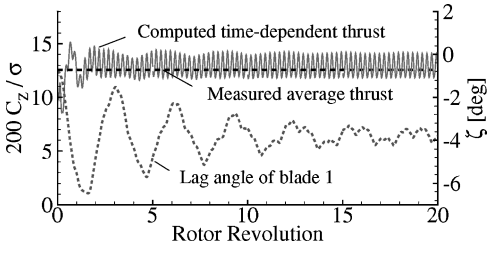


**Fig. 10 Time history of rotor thrust and blade lag angle in forward flight.**

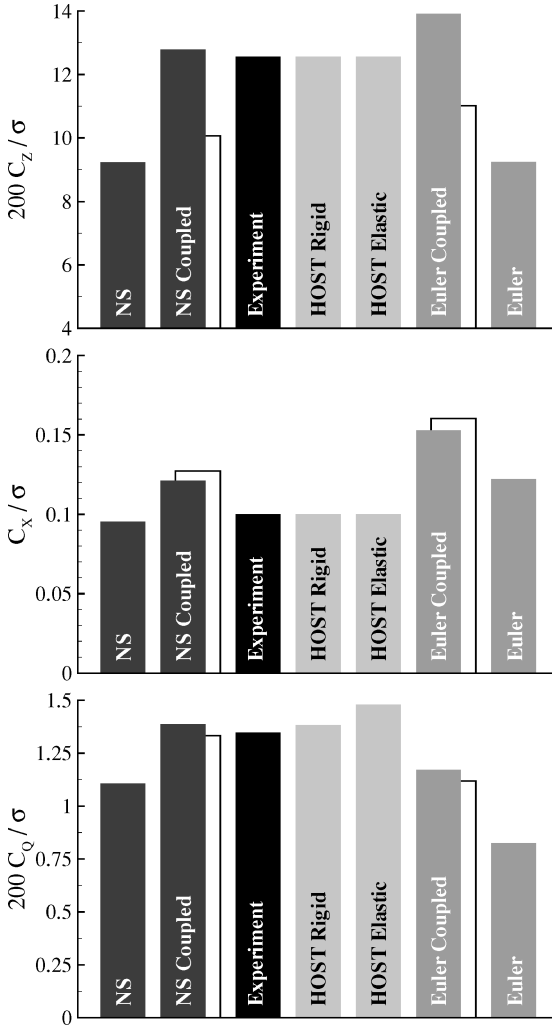


**Fig. 11 Computed and measured rotor coefficients in forward flight.**

tilt angles underestimate the experimental rotor thrust[12] by approximately 25%. Much better agreement is achieved using the coupled Navier–Stokes analysis, which predicts a vertical force merely 1.8% above the measurements.[12] Note that the thrust values computed by the uncoupled inviscid and viscous analyses are nearly identical, whereas the results of the coupled computations differ by approximately 9%, which indicates significant differences between Euler and Navier–Stokes regarding the predicted blade motion and/or elastic deformation. Although in much better agreement with the wind-tunnel data than the Euler result, the coupled hybrid analysis is found to underestimate the overall drag, which may be due in part to the missing rotor head in the numerical simulation. The rotor torque coefficient computed by the coupled hybrid analysis is approximately 6% below the prediction of the corresponding HOST soft blade trim computation and within 3% of the experimental value. Additional coupled computations are carried out using the experimental values for $\alpha_q$ and $\theta(\psi)$, and the resulting global rotor coefficients are represented by the white bars in the background of Fig. 11. Because the coupled results obtained with the HOST control parameters are found to correlate much better with the experimental data, only the output of these calculations will be discussed beyond this point.

In Fig. 12, computed and measured normal force coefficients are plotted over $\psi$ for a number of radial stations. The rigid blade CFD analysis with fully prescribed hinge angles taken from the corresponding HOST trim calculation is found to reproduce the principal characteristics of the experimental data,[26] although with significant deviations in phase and amplitude. For comparison, results of a rigid-blade computation in which the control input is limited to $\alpha_q$ and $\theta(\psi)$ are included in Fig. 12 to emphasize especially the impact of the flap degree of freedom on the aerodynamic coefficients.

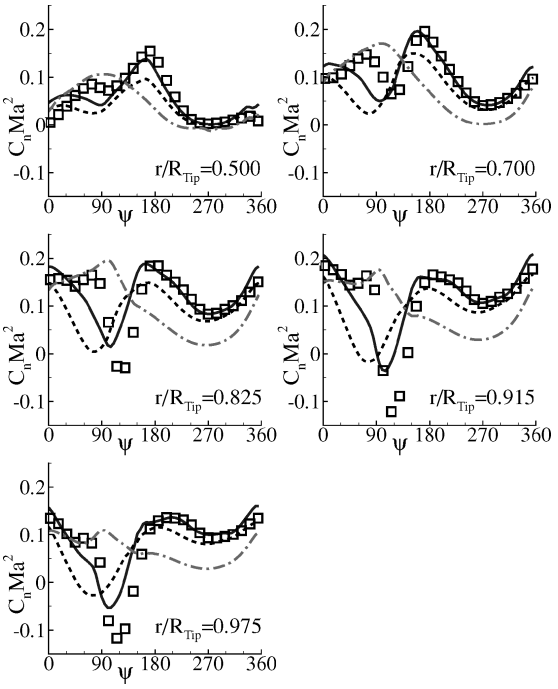


**Fig. 12 Computed sectional normal forces compared with experiment: – · –, NS $\alpha_q$, $\theta(\psi)$; - - - -, NS; ——, coupled; and □, experiment.**

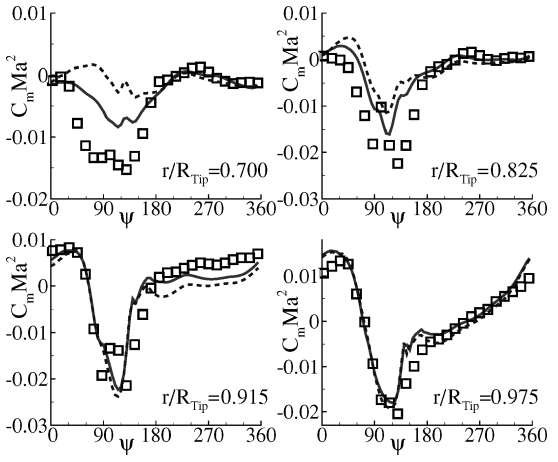


**Fig. 13 Computed and measured pitching moment: ——, NS coupled; - - - -, Euler coupled; and □, experiment.**

Qualitatively and quantitatively, the normal forces computed by the coupled analysis correlate quite well with the experimental data. A moderate phase shift can be observed between the peaks of the computed and measured curves. The characteristic dip in the tip region at around 120-deg blade azimuth is captured (yet underestimated) by the hybrid aeroelastic analysis, whereas the measured local normal force maximum preceding it is only reproduced as a trend in the present numerical results.

A comparison of the computed local pitching moment coefficients with experimental data of ONERA is given in Fig. 13. At $0.7 \times R_{\text{tip}}$, the negative pitching moment measured on the advancing side of the rotor is reproduced, but underpredicted by the viscous analysis, whereas the Euler simulation returns positive values over the first-quarter revolution. Toward the blade tip, the computed sectional pitching moments correlate well with the experimental data and slight advantages of the Navier–Stokes model over the inviscid analysis are visible at 82.5 and 91.5% blade radius.

Chordwise pressure distributions at 97.5% tip radius are presented in Fig. 14 in 30-deg azimuthal increments. The results of the hybrid aeroelastic analysis correlate well with experimental data.[26] The ability of the procedure to capture unsteady transonic effects ade-

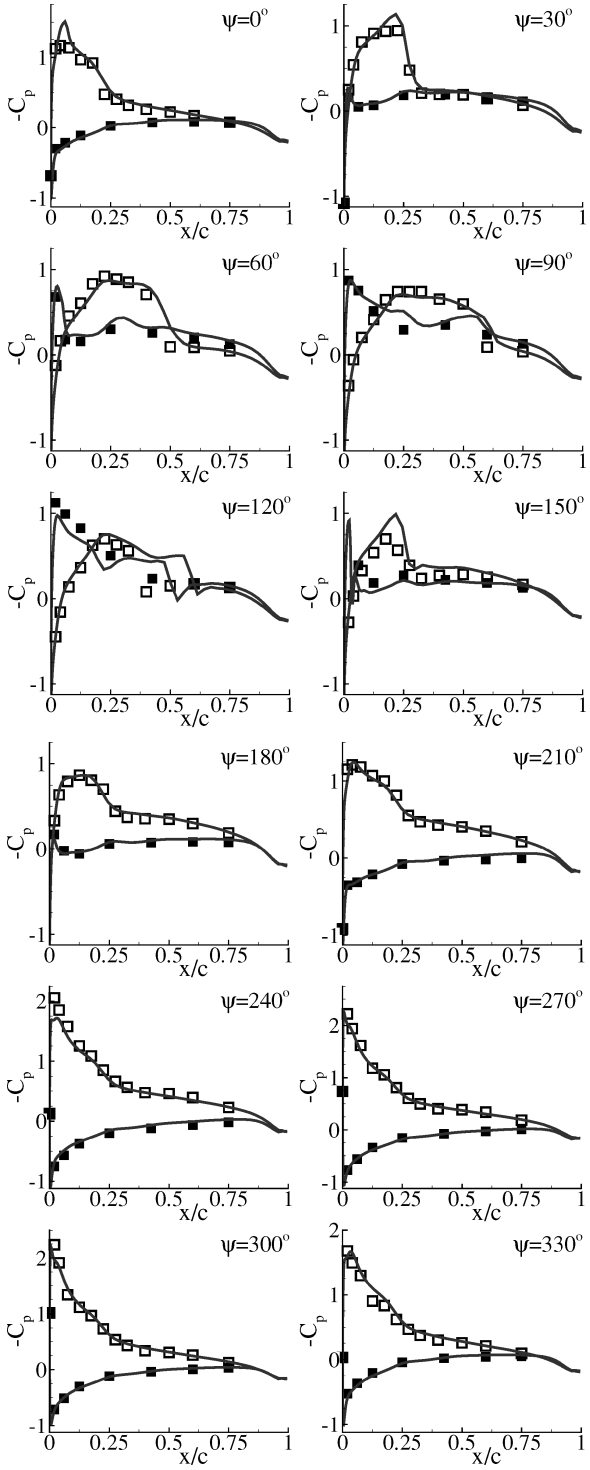


**Fig. 14 Pressure coefficients at 97.5% $R_{\text{tip}}$: ——, NS coupled and ■/□, experiment (lower/upper).**

quately is clearly demonstrated. Because of the high advance ratio of the selected test case, a strong shock builds up on the upper surface between 0 and 30-deg blade azimuth. The predicted shock positions vary between $0.25 \times c$ and $0.60 \times c$, and the most significant discrepancies between simulation and experiment can be noticed in the course of the shock breakdown, whereas very good agreement is observed on the entire retreating side of the rotor in the proximity of the tip. On the retreating side, correlation of numerical and experimental data is found to deteriorate further inboard, where a huge region of reverse flow and very low dynamic pressure must be dealt with by the compressible flow solver. Furthermore, the algebraic eddy viscosity model used in the present viscous analysis is unable

to predict accurately the dynamic stall phenomenon encountered in the central portion of the retreating blade, which is imperative to obtain a realistic representation of the unsteady blade loads in this azimuthal range.

Finally, note stated that the results of the first principles-based forward flight computations presented in this paper are a fairly good approximation, but not an exact representation of the fully trimmed rotor state. The rolling moment of the rotor predicted by the aeroelastic hybrid analysis corresponds to a lateral offset of the rotor thrust of approximately $0.01 \times R_{\text{tip}}$. Recall that the primary rotor controls used throughout the coupled CFD simulations are based on the simplified aerodynamics included in the HOST trim analysis. Further improvement of the agreement between numerical and experimental data may be achieved, at tremendous computational cost, by incorporating a trim capability within the aeroelastic analysis where the rotor trim provided by HOST is used as an initial solution.

## Conclusions

We presented a numerical approach for the aeroelastic analysis of helicopter rotors in hover and forward flight based on the RANS equations and Timoshenko beam theory in conjunction with a staggered coupling scheme.

The global thrust and torque coefficients predicted by the hybrid aeroelastic chimera analysis for the 7A model rotor hovering at a moderate thrust setting were within the available experimental databands. In the fully turbulent analysis, good agreement between simulation and measurements was achieved for the evolving rotor figure of merit, whereas an attempt to take into account laminar–turbulent transition was found to lead to a significant overestimation of this quantity. The inclusion of a hub model in the analysis and the application of a more advanced turbulence model may help to further improve the correlation of numerical and experimental hover performance data.

Global and local aerodynamic loads computed by the strongly coupled hybrid analysis for a high-speed forward flight test case provided fairly good agreement with the measurements, and the ability of the procedure to compute quite accurately strong unsteady compressibility effects and to reproduce essential blade deformation characteristics could be demonstrated. Compared with uncoupled simulations using prescribed rigid-blade articulation, the viscous aeroelastic analysis was found to correlate far better with the experimental data and also showed advantages over a coupled inviscid computation with respect to sectional pitching moment prediction.

## Acknowledgments

This work has been supported by Deutsche Forschungsgemeinschaft under reference code Wa424/14. The authors would like to thank A. Fischer [Institute for Aerodynamics and Gasdynamics (IAG)] for the numerous technical discussions and to acknowledge the support of A. Altmikus (IAG) and ONERA Châtillon regarding selected experimental and HOST trim data for the 7A model rotor provided for validation tasks in the framework of the French–German complete helicopter advanced computational environment (CHANCE) project. Finally, the authors would like to acknowledge the high performance computing (HPC) support of H. Berger and M. Galle (both NEC European Supercomputer Systems).

## References

[1]Wagner, S., "Flow Phenomena on Rotary Wing Systems and their Modeling," *ZAMM Zeitschrift für Angewandte Mathematik und Mechanik*, Vol. 79, No. 12, 1999, pp. 795–820.

[2]Krämer, E., "Theoretische Untersuchungen der stationären Rotorblattumströmung mit Hilfe eines Euler–Verfahrens," Ph.D. Dissertation, Univ. of the German Army, Inst. for Aeronautics and Aircraft Structures, Fortschritt–Berichte VDI, Reihe 7, Munich, No. 197, July 1991.

[3]Boniface, J.-C., and Sidès, J., "Numerical Simulation of Steady and Unsteady Euler Flows around Multibladed Helicopter Rotors," *Proceedings of the 19th European Rotorcraft Forum*, Vol. 1, Associazione Italiana di Aeronautica e Astronautica, Italy, 1993, pp. C10-1–C10-21.

[4]Stangl, R., "Ein Euler–Verfahren zur Berechnung der Strömung um einen Hubschrauber im Vorwärtsflug," Ph.D. Dissertation, Univ. of Stuttgart, Inst. of Aerodynamics and Gas Dynamics, Stuttgart, Germany, Oct. 1996.

[5]Wake, B. E., and Baeder, J. D., "Evaluation of a Navier–Stokes Analysis Method for Hover Performance Prediction," *Journal of the American Helicopter Society*, Vol. 41, No. 1, 1996, pp. 1–17.

[6]Wehr, D., "Untersuchungen zum Wirbeltransport bei der Simulation der instationären Umströmung von Mehrblattrotoren mittels der Euler–Gleichungen," Ph.D. Dissertation, Univ. of Stuttgart, Inst. of Aerodynamics and Gas Dynamics, Stuttgart, Germany, March 1999.

[7]Strawn, R. C, and Ahmad, J. U., "Computational Modeling of Hovering Rotors and Wakes," AIAA Paper 2000-0110, Jan. 2000.

[8]Beaumier, P., Pahlke, K., and Chelli, E., "Navier–Stokes Prediction of Helicopter Rotor Performance in Hover Including Aero-Elastic Effects," *Annual Forum Proceedings*, Vol. 1, American Helicopter Society, Alexandria, VA, 2000, pp. 391–401.

[9]Strawn, R. C., and Djomehri, M. J., "Computational Modeling of Hovering Rotor and Wake Aerodynamics," *Proceedings of the AHS 57th Annual Forum*, American Helicopter Society, Alexandria, VA, 2001.

[10]Friedmann, P. P., "Rotary–Wing Aeroelasticity–Current Status and Future Trends," AIAA Paper 2001-0427, Jan. 2001.

[11]Altmikus, A., Wagner, S., Hablowetz, T., and Well, K., "On the Accuracy of Modular Aeroelastic Methods Applied to Fixed and Rotary Wings," AIAA Paper 2000-4224, Aug. 2000.

[12]Servera, G., Beaumier, P., and Costes, M., "A Weak Coupling Method between the Dynamics Code HOST and the 3D Unsteady Euler Code WAVES," *Proceedings of the 26th European Rotorcraft Forum* [CD-ROM], The Netherlands Association of Aeronautical Engineers, The Hague, The Netherlands, 2000.

[13]Pahlke, K., and van der Wall, B., "Calculation of Multibladed Rotors in High–Speed Forward Flight with Weak Fluid–Structure–Coupling," *Proceedings of the 27th European Rotorcraft Forum* [CD-ROM], Kamov Co., Moscow, Russia, 2001.

[14]Hierholz, K., "Ein numerisches Verfahren zur Simulation der Strömungs–Struktur–Kopplung am Hubschrauberrotor," Ph.D. Dissertation, Univ. of Stuttgart, Inst. of Aerodynamics and Gas Dynamics, Stuttgart, Germany, Nov. 1999.

[15]Buchtala, B., "Gekoppelte Berechnung der Dynamik und Aerodynamik von Drehflüglern," Ph.D. Dissertation, Univ. of Stuttgart, Inst. of Aerodynamics and Gas Dynamics, Stuttgart, Nov. 2002.

[16]Pomin, H., and Wagner, S., "Navier–Stokes Analysis of Helicopter Rotor Aerodynamics in Hover and Forward Flight," AIAA Paper 2001-0998, Jan. 2001.

[17]Baldwin, B. S., and Lomax, H., "Thin Layer Approximation and Algebraic Model for Separated Turbulent Flow," AIAA Paper 78-0257, 1978.

[18]Eberle, A., "MBB–EUFLEX. A New Flux Extrapolation Scheme Solving the Euler Equations for Arbitrary 3-D Geometry and Speed," Rept. MBB/LKE122/S/PUB/140, MBB, Ottobrun, Germany, 1984.

[19]Jameson, A., and Yoon, S., "LU Implicit Schemes with Multiple Grids for the Euler Equations," AIAA Paper 86-0105, Jan. 1986.

[20]Pomin, H., and Wagner, S., "Navier–Stokes Analysis of Isolated Rotor Flow in Helicopter Hover Flight," *Proceedings of the European Congress on Computational Methods in Applied Sciences and Engineering (ECCOMAS 2000)* [CD-ROM], International Center of Numerical Methods in Engineering (CIMNE), Barcelona, 2000.

[21]Chung, J., and Hulbert, G. M., "A Time Integration Algorithm for Structural Dynamics with Improved Numerical Dissipation: The Generalized–$\alpha$ Method," *Journal of Applied Mechanics*, Vol. 60, No. 2, 1993, pp. 371–375.

[22]d'Alascio, A., Pahlke, K., Castellin, C., and Costes, M., "Aerodynamics of Helicopter. Application of the Navier–Stokes Codes Developed in the Framework of the Joint German/French CFD Research Program CHANCE," *Proceedings of the 27th European Rotorcraft Forum* [CD-ROM], Kamov Co., Moscow, Russia, 2001.

[23]Schultz, K.-J., Splettstößer, W., Junker, B., Wagner, W., Schöll, E., Arnaud, G., Mercker, E., Pengel K., and Fertis, D., "A Parametric Wind Tunnel Test on Rotorcraft Aerodynamics and Aeroacoustics (HELISHAPE)—Test Documentation and Representative Results," Inst. für Entwurfsaerodynamik, Rept. IB 129-96/25, DLR, German Aerospace Research Center, Brunswick, Germany, 1996.

[24]Jeong, J., and Hussain, F., "On the Identification of a Vortex," *Journal of Fluid Mechanics*, Vol. 285, 1995, pp. 69–94.

[25]Benoit, B., Dequin, A.-M., Kampa, K., Grunhagen, W., Basset, P.-M., and Gimonet, B., "HOST, A General Helicopter Simulation Tool for Germany and France," *Proceedings of the AHS 56th Annual Forum*, American Helicopter Society, Alexandra, VA, 2000.

[26]Pahlke, K., and Chelli, E., "Calculation of Multibladed Rotors in Forward Flight Using a 3D Navier–Stokes Method," *Proceedings of the 26th European Rotorcraft Forum* [CD-ROM], The Netherlands Association of Aeronautical Engineers, The Hague, The Netherlands, 2000.